Xinghua Shi
e-mail: shixh@imech.ac.cn

Qifang Yin

State Key Laboratory of Nonlinear Mechanics,
Institute of Mechanics,
Chinese Academy of Sciences,
Beijing 100190, China

Nicola M. Pugno
Laboratory of Bio-Inspired and Graphene Nanomechanics,
Department of Civil, Environmental and Mechanical Engineering,
University of Trento via Mesiano,
77 Trento, I-38123 Italy

Huajian Gao
School of Engineering,
Brown University,
610 Barus & Holley,
182 Hope Street,
Providence, RI 02912
e-mail: huajian_gao@brown.edu

Tunable Mechanical Behavior of Carbon Nanoscroll Crystals Under Uniaxial Lateral Compression

A theoretical model is developed to investigate the mechanical behavior of closely packed carbon nanoscrolls (CNSs), the so-called CNS crystals, subjected to uniaxial lateral compression/decompression. Molecular dynamics simulations are performed to verify the model predictions. It is shown that the compression behavior of a CNS crystal can exhibit strong hysteresis that may be tuned by an applied electric field. The present study demonstrates the potential of CNSs for applications in energy-absorbing materials as well as nanodevices, such as artificial muscles, where reversible and controllable volumetric deformations are desired. [DOI: 10.1115/1.4024418]

1 Introduction

Graphene-based carbon nanoscrolls (CNSs), also referred to as buckyrolls, have attracted significant interest in recent years [1–6] due to their unique structural [7–11], dynamical [9], and electronic [2,7,12,13] properties. In contrast to carbon nanotubes (CNTs), the core size of the CNSs can be tuned by changing system parameters such as the effective surface energy via an applied electric field [14–16], which makes it a natural choice for a new class of efficient nanoacutators [10,17–20] or materials for possible hydrogen storage [9–11]. Recent experiments on electrical-transport measurements [2] showed that the electrical resistance of a CNS is weakly gate dependent but strongly temperature dependent. In addition, CNSs can sustain a high current density, making them potentially a good candidate for microcircuit interconnects.

The promising applications of CNSs in nanotechnology have stimulated growing research interest in this area. So far, most previous studies on CNSs have been focused on fabrication [1–6], electronic properties [7,12,13], and dynamic behaviors [8,16,21], as well as deformation characteristics [22–24]. Their flexible configuration in the radial direction enables CNSs to undergo large deformations under relatively small loadings, which is most distinct from that of CNTs. An open question is how mechanical loading influences the behavior of a bundle of closely packed CNSs forming a macromolecular crystal. The present paper is dedicated to investigating the mechanical behavior of a CNS crystal under uniaxial compression/decompression via both theoretical modeling and molecular dynamics (MD) simulations.

2 Theoretical Model

Consider a graphene sheet of length B and width b that is rolled up into a CNS with inner core radius r_0, outer radius R, and interlayer spacing h. A large number (N) of such CNSs can be packed to form a crystal. For simplicity, we consider a closely packed CNS crystal with scroll axes parallel to the out-of-plane direction. The CNSs are closely packed so that each CNS has six nearest neighbors. Under external uniaxial compression, the pressure applied to the crystal is p and we ignore possible pressure inside the inner core of the nanoscrolls (Fig. 1). What is the aggregate deformation behavior of such a CNS crystal?

In a previous paper we studied the mechanical behavior of an individual or a bundle of CNSs undergoing radial contraction/expansion under axisymmetric pressure [24]. Here we consider the deformation of a CNS crystal under uniaxial compression that involves nonaxisymmetrical deformation as shown in Fig. 1. In this situation, the CNS no longer has the usual (approximately) axisymmetric spiral form. Our MD simulations to be discussed shortly will show that the graphene layers of CNSs perpendicular to the compressing direction are forced to contact each other with a flat contact region with length L during deformation (the blue

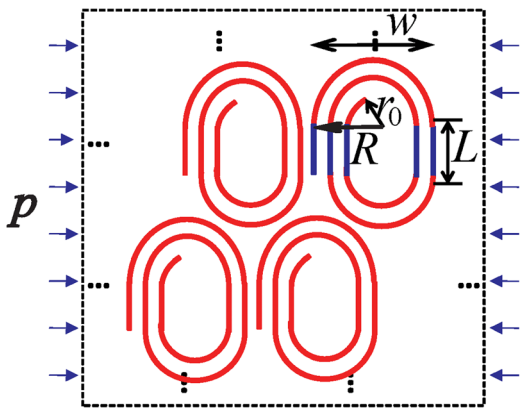

Fig. 1 Schematic illustration of a crystal of carbon nanoscrolls with inner core radius r_0, outer radius R and interlayer spacing h under uniaxial compression

Contributed by the Applied Mechanics Division of ASME for publication in the JOURNAL OF APPLIED MECHANICS. Manuscript received April 2, 2013; final manuscript received April 26, 2013; accepted manuscript posted May 7, 2013; published online September 16, 2013. Editor: Yonggang Huang.

line in Fig. 1). For each CNS, assume there are n layers of graphene in the flat contact region, while the remaining parts still form an approximately circular scroll (the red part of Fig. 1). In this configuration, conservation of the total area of a CNS suggests

$$(B - nL)h = \pi\left(R^2 - r_0^2\right) \tag{1}$$

The in-plane width of the CNS is

$$w \approx 2R = 2r_0 + \frac{2n-3}{2}h \tag{2}$$

Following our previous analysis of a single CNS [19], the potential energy of the above compressed CNS system is

$$E = \frac{Nb\pi D}{h}\ln\left(\frac{R}{r_0}\right) + 2Nb\gamma(\pi r_0 + \eta\pi R + L) + 2NbpR(L + 2R) \tag{3}$$

where the first term is associated with the bending energy of CNS and D is the bending modulus of graphene, which has the same dimension as energy; the second term is associated with the surface energy and γ is the surface energy per unit area, $\eta \approx 1$ implies a nearly circular shape of the nanoscrolls, and $\eta \approx 0$ for fully collapsed CNSs [25]; the third term is associated with mechanical work by the applied pressure. Normalizing all length parameters by h and energy by D, Eq. (3) is recast as

$$\bar{E} = N\bar{b}\pi\ln\left(\frac{\bar{R}}{\bar{r}_0}\right) + 2N\bar{b}\bar{\gamma}(\pi\bar{r}_0 + \eta\pi\bar{R} + \bar{L}) + 2N\bar{b}\bar{p}\bar{R}(\bar{L} + 2\bar{R}) \tag{4}$$

where

$$\bar{E} = \frac{E}{D},\quad \bar{\gamma} = \frac{\gamma h^2}{D},\quad \bar{p} = \frac{ph^3}{D},\quad \bar{b} = \frac{b}{h},\quad \bar{r}_0 = \frac{r_0}{h},\quad \bar{R} = \frac{R}{h},\quad \bar{L} = \frac{L}{h},\quad \bar{B} = \frac{B}{h}$$

Eq. (4) contains four unknown variables: $\bar{r}_0, \bar{R}, \bar{L}, n$, with the other parameters being constant. To solve Eq. (4), we minimize the potential energy $\bar{E}$ with respect to the core radius $\bar{r}_0$ as well as the contact length at equilibrium

$$\frac{\partial\bar{E}}{\partial\bar{r}_0} = 0 \tag{5a}$$

$$\frac{\partial\bar{E}}{\partial\bar{L}} = 0 \tag{5b}$$

Combining Eqs. (1), (2), and (5) leads to minimization of the potential energy in Eq. (4). Figure 2 plots the numerical solution for the contact layer number n as a function of the applied pressure. Interestingly, our model predicts that n varies mildly as the pressure increases, suggesting that there is little core contraction due to interlayer sliding during uniaxial compression. Consequently, the main deformation mode seems to be dominated by the bending of the multilayered graphene walls of the CNSs. We will show shortly that this is fully corroborated by our MD simulations. Figure 2 shows the typical behaviors of the contact layer number n under increasing compression. Here the parameter $\bar{B} = 270$ is fixed while $\bar{\gamma}$ and η are tuned. We note that $\bar{\gamma} = 0.136$ is a typical value for graphene with $h = 0.34$ nm, $D = 0.17$ nmnN, and $\gamma = 0.2$ nN/nm.

The above result suggests that we can go back to Eqs. (1)–(3) and simplify the problem by assuming n to be a constant. Writing Eqs. (1) and (2) in differential form, we obtain $dR = dr_0$, $dL = -2\pi(RdR - r_0dr_0)/nh \approx -\pi dr_0$. Then Eq. (5a) is recast as

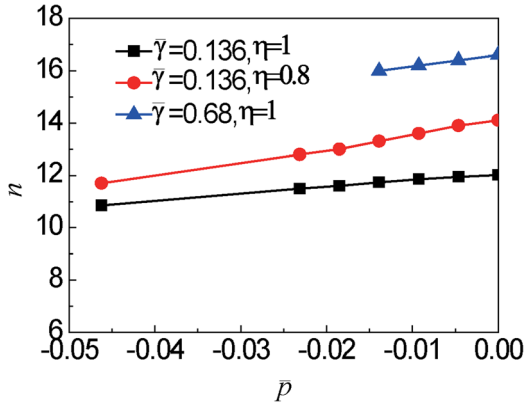

Fig. 2 Variation of the contact layer number n with the increasing compressive stress $\bar{p}$, where n decreases mildly as $\bar{p}$ increases. The parameters adopted in the calculations are $\bar{B} = 270$, $\bar{\gamma} = 0.136$, $\eta = 1$ (black), $\bar{\gamma} = 0.136$, $\eta = 0.8$ (red), and $\bar{\gamma} = 0.68$, $\eta = 1$ (blue).

$$\pi\left(\frac{1}{\bar{R}_e} - \frac{1}{\bar{r}_{0e}}\right) + 2\pi\bar{\gamma}\eta + 2\bar{p}(\bar{L}_e + 4\bar{R}_e - \pi\bar{R}_e) = 0 \tag{6}$$

where subscript "e" stands for equilibrium. This equation and Eq. (1) yield

$$\bar{p}(R_e) = -\frac{\pi}{2(\bar{L}_e + 4\bar{R}_e - \pi\bar{R}_e)}\left(2\eta\bar{\gamma} - \frac{1}{\bar{r}_{0e}} + \frac{1}{\bar{R}_e}\right)$$

$$\bar{r}_{0e} = \sqrt{\bar{R}_e^2 - \frac{\bar{B} - n\bar{L}_e}{\pi}} \tag{7}$$

Setting $\bar{p} = 0$ in Eq. (7) gives the following equation to determine n from:

$$\bar{B} = \sqrt{\frac{\pi^2 n^3(1 + \bar{\gamma}\eta/4)}{4\bar{\gamma}\eta}} \tag{8}$$

The equilibrium radius $\bar{R}_e$ can be calculated from Eq. (7), and the total volume of the crystal is

$$\bar{V} = V/h^3 = 2N\bar{R}_e(2\bar{R}_e + \bar{L}_e)\bar{b} \tag{9}$$

3 Molecular Dynamics Simulations

MD simulations are performed to verify the above theoretical model. The periodic boundary condition is applied along all dimensions. The adaptive intermolecular reactive empirical bond order (AIREBO) potential [26] is used to describe the bonded interaction between carbon atoms. The simulations are performed based on the large-scale atomic/molecular massively parallel simulator (LAMMPS) [27] code, with a constant time step of 1 fs and the NPT ensemble (i.e., constant number of atoms, constant pressure $P = 0$ bar, and constant temperature $T = 10$ K). Prior to loading, each sample is relaxed to its equilibrium state with almost zero pressure. Uniaxial compression/decompression at a strain rate of $10^8\,\mathrm{s}^{-1}$ is then applied in the horizontal direction while the box is allowed to shrink in the vertical direction (LAMMPS; Ref. [27] command: fix/deform). The nonbonded van der Waals (vdW) interactions between carbon atoms are described by the Lennard–Jones (LJ) potential

$$U(r_{ij}, \lambda) = 4\lambda\varepsilon_{CC}\left[\left(\frac{\sigma_{CC}}{r_{ij}}\right)^{12} - \left(\frac{\sigma_{CC}}{r_{ij}}\right)^{6}\right] \tag{10}$$

where $\varepsilon_{CC} = 2.8437$ meV, $\sigma_{CC} = 0.34$ nm, and λ is a scaling parameter $(0 < \lambda \leq 1)$ for the nonbonded interactions between

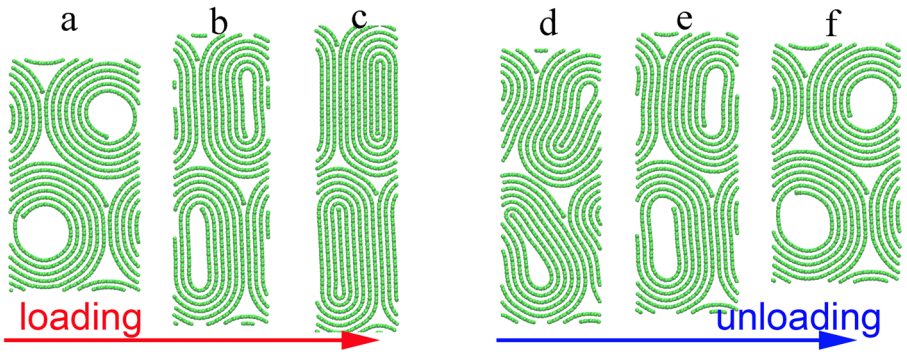

Fig. 3 Snapshots of MD simulation results showing the evolution of a CNS crystal under uniaxial compression/decompression

carbon atoms. Experimentally, the tuning of interaction parameter λ can be realized by applying an electric field to reduce the effective surface energy of the CNSs [15].

4 Results and Discussions

During uniaxial compression, MD simulations show that the CNS crystal under investigation is forced to contract in the horizontal direction while extending in the vertical direction (Figs. 3(*a*)–3(*c*)). The cores of the CNSs undergo a suddenly collapse at a critical stage of contraction (Figs. 3(*b*) and 3(*c*)), somewhat similar to the collapse of single-walled carbon nanotubes (CNTs) [25,28–32] due to the vdW attraction between carbon atoms near the inner core. During decompression, the cores of the CNSs suddenly open up (Figs. 3(*d*) and 3(*e*)) to release the elastic bending energy stored in the crystal. It is observed that the CNS crystal recovers its initial state as the applied pressure is removed (Figs. 3(*d*)–3(*f*)). During the compression/decompression, the layer number n of the CNS crystal remains almost constant, corroborating our model prediction shown in Fig. 2 and indicating negligible interlayer sliding during deformation.

It has been shown that the critical condition for the self-collapse of CNTs [25,28–32] into a dog-bone structure depends on the radius of the most inner tube and the intrinsic material properties in the form $r \geq r_{\text{collapse}} = \sqrt{(3D/\gamma)(n/2)^{\alpha}}$, while the self-recovery from the dog-bone structure requires $r \leq r_{\text{recovery}} = \sqrt{(2D/\gamma)(n/2)^{\alpha}}$ [25]. Here α is a scaling parameter in the range $1 \leq \alpha \leq 3$ tuning the bending modulus of CNT walls. For a CNS, the aggregate bending modulus of its wall should scale linearly with the number of layers, in which case $\alpha = 1$. This is a distinct feature making CNSs different from CNTs, which enables CNSs to be much more deformable than CNTs of comparable size under unaxial lateral compression. To investigate if CNSs would self-collapse and self-recover, we calculate the inner core size of the CNSs by setting $\bar{p} = 0$ in Eq. (7). Figure 4(*a*) shows that the normalized core size of the CNSs varies with the length of the basal graphene sheet, which is in turn related to the number of rolling layers, where the other system parameters are taken as $\gamma = 0.136\ \lambda$ and $\eta = 1$. It is seen that the core size of the CNSs is always smaller than r_{collapse} as n increases, suggesting that the CNSs would never self-collapse. Also, the core size is found to be always smaller than r_{recovery}, indicating that the CNSs can self-recover from the dog-bone structure once the applied load is released. Tuning the surface energy by decreasing the parameter λ would not change the trend (Fig. 4(*b*)). We note that our MD results are consistent with our model predictions. Note that these features associated with the self-collapse/recovery of CNSs are distinct from those of CNTs and suggest that CNSs are a promising candidate for energy-adsorbing materials.

In MD simulations, the pressure is calculated from the net force in the loading direction acting on the box boundary (i.e., force averaged over all the boundary atoms) and then compared to our theoretical predictions. The stress-strain curve in Fig. 5(*a*) shows two apparent steps during compression/decompression of the CNS crystal: One indicates the occurrence of a pull-in instability (in blue) and the other a snap-open instability (in green). The resulting hysteresis loop during compression/decompression indicates the amount of energy dissipation per unit volume. With appropriate parameters selected as those in our MD simulations, i.e., $\bar{B} = 270$, $\bar{\gamma} = 0.136\lambda$, Fig. 5(*a*) shows the theoretical predictions for different values of η. It is seen that the theoretical prediction corresponding to $\eta = 0.4$ fits the MD results well before the pull-in instability occurs. Due to the hysteretic behavior, our

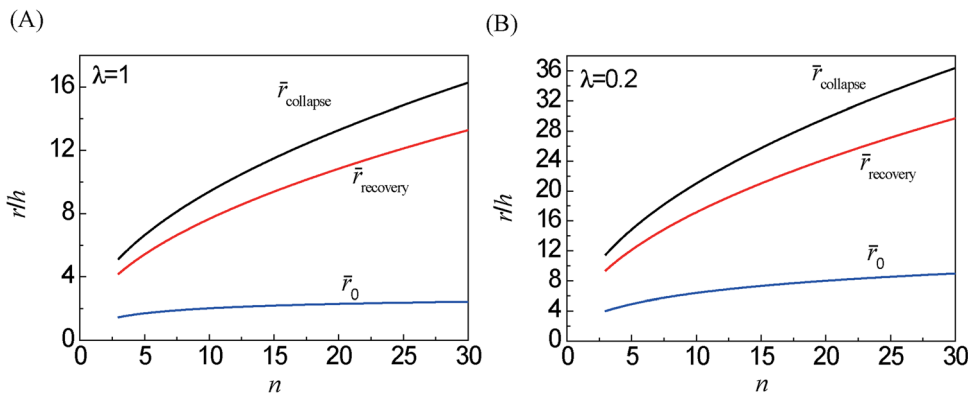

Fig. 4 The core size of CNSs normalized by *h* as a function of the number of layers. For comparison, the critical sizes normalized by *h* associated with self-collapse and self-recovery for CNTs are shown as black and red lines, respectively. Other system parameters are taken to be $\bar{\gamma} = 0.136\lambda$, $\eta = 1$ and (*a*) $\lambda = 1$, (*b*) $\lambda = 0.2$.

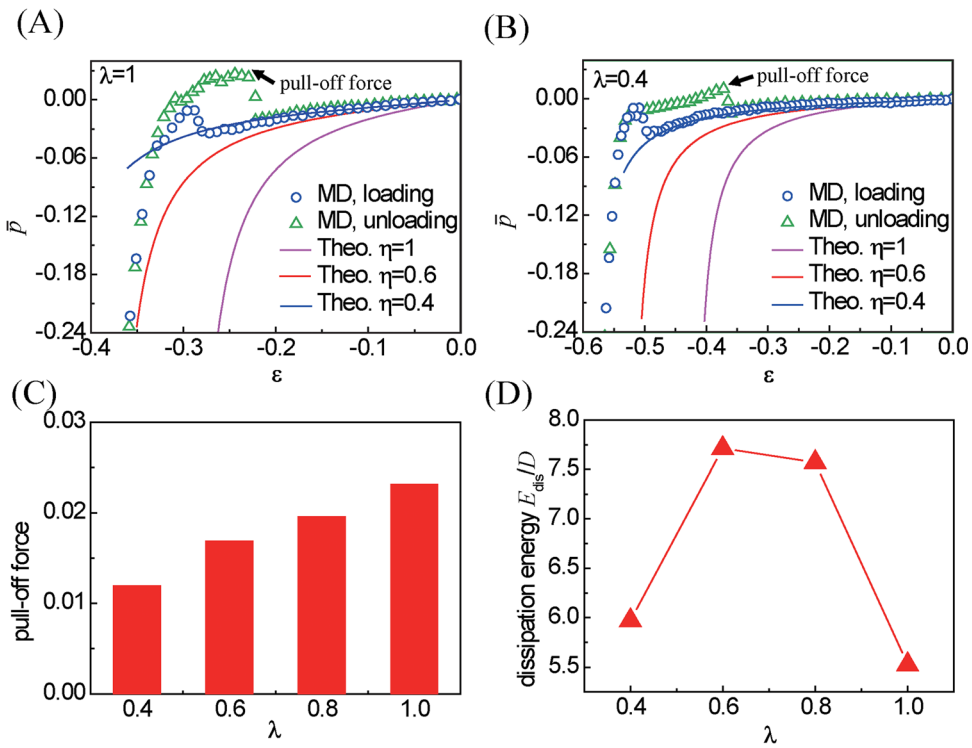

Fig. 5 Stress-strain profiles of the CNS crystal under uniaxial compression (blue circles)/decompression (green triangles) under different LJ energy tuning parameter (*a*) $\lambda = 1$ and (*b*) $\lambda = 0.4$. The solid lines indicate theoretical results with parameters $\bar{B} = 270$, $\bar{\gamma} = 0.136\lambda$, $\eta = 0.4$ (blue), 0.6 (red), 1 (magenta) and $\eta = 12$ for $\lambda = 1$, $\eta = 10$ for $\lambda = 0.4$. (*c*) The normalized pull-off force (see arrows in Figs. 5(*a*) and 5(*b*)) for CNSs to recover from the collapsed state under different values of the LJ energy tuning parameter λ. (*d*) The normalized energy dissipated during a loading-unloading cycle under different values of the LJ energy tuning parameter λ.

theoretical model cannot fit the MD results after the pull-in instability occurs (Fig. 5(*a*), blue line).

To further investigate how the electric field influences the hysteresis behavior of a CNS crystal, we tune the LJ energy factor λ to 0.8, 0.6, and 0.4. It is seen that the height of the hysteresis loop decreases while the width increases with a growing λ (Fig. 5(*b*)). The height of the hysteresis loop is mainly controlled by the pull-off force, which is defined as the tension (negative pressure) on the CNS as the snap-open instability occurs (see the arrow in Fig. 5(*a*)). The measured pull-off forces for different values of λ are listed in Fig. 5(*c*). The pull-off force increases almost linearly with λ, which could be understood from the fact that λ scales linearly with the vdW interaction energy as shown in Eq. (10). The width of the hysteresis loop, however, is mainly controlled by the size of the inner core of CNS, which decreases as λ is reduced. So the area of the hysteresis loop, roughly the product of height and width, does not necessarily vary monotonically with λ. Interestingly, the calculated dissipation energy first increases and then decreases with λ, indicating that there exists an optimal surface energy for maximum dissipation.

The length of the basal graphene that rolls into the CNSs can also influence the compressive behavior of the CNS crystal. Here we theoretically investigate the length effect by changing the $\bar{B}$ in Eq. (7). Figure 6 shows the stress-strain curves for $\bar{B} = 270$ (in blue) and $\bar{B} = 2700$ (in red), with the other parameters fixed at $\bar{\gamma} = 0.136$, $\eta = 0.4$. It is seen that the slope of stress-strain curve increases with the increase of $\bar{B}$, indicating that the CNS crystal becomes more rigid as $\bar{B}$ increases. This could be understood from the fact that the rolling number n increases with $\bar{B}$, which tends to enhance the total bending rigidity of graphene layers and, hence, the effective stiffness under uniaxial lateral compression.

In the MD simulations we have selected a strain rate of $10^8\ s^{-1}$ to compress the CNS crystal. To investigate how the strain rate

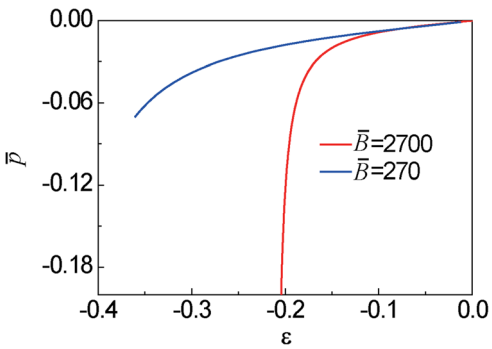

Fig. 6 Stress-strain profiles of a CNS crystal under uniaxial lateral compression with different lengths of the basal graphene that rolls into individual CNSs

affects the result in our system, we have done additional simulations at a strain rate one order of magnitude higher. As shown in Fig. 7(*a*), the obtained stress-strain curve does not change substantially, except that the stress increases slightly faster as the CNS becomes packed, indicating that the rate effect is limited in the system under study.

Since CNSs have a multilayered structure somewhat similar to that of multiwalled carbon nanotubes, one would be interested in the difference in their behaviors under unaxial lateral compression. Our simulations indicate that the main difference lies with their large differences in rigidity. As stated above, for CNSs the rigidity is proportional to the number of layers in the CNSs, i.e., $D_{\text{total}} \propto n/2$. For CNTs, however, it is scaled as $D_{\text{total}} \propto (n/2)^{\alpha}$ where $1 < \alpha \leq 3$. We have conducted additional simulations by setting up a similar system containing multiwalled CNTs crystal.

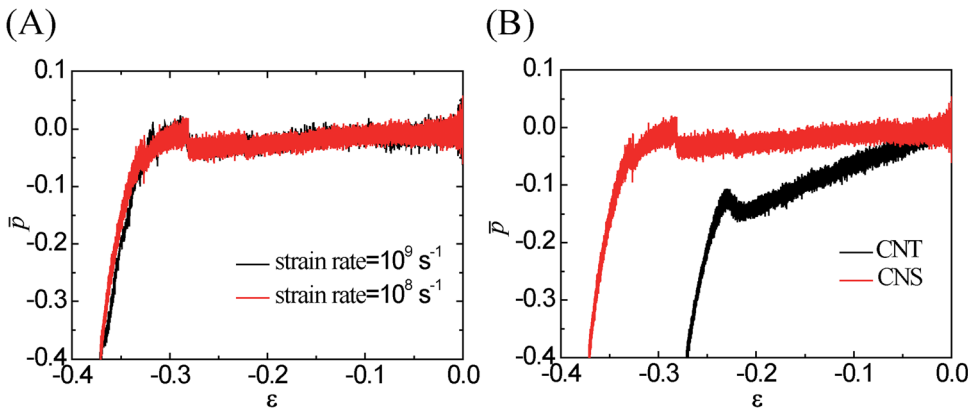

Fig. 7 Comparison of the stress-strain profiles for (*a*) CNS compressed under different strain rate and (*b*) CNTs and CNSs under uniaxial lateral compression

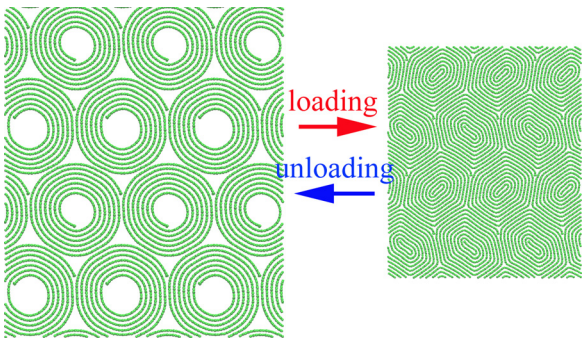

Fig. 8 Snapshots of MD simulation results showing the initial and final states of a CNS crystal under equibiaxial compression/decompression

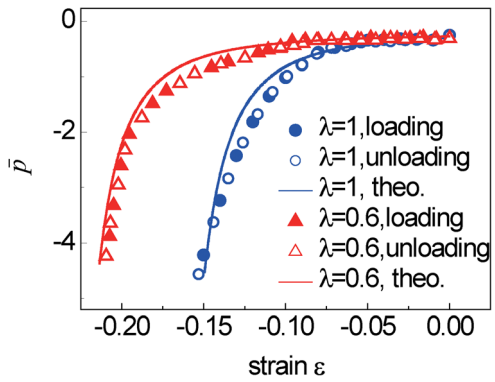

Fig. 9 Stress-strain profiles of CNSs under biaxial compression/decompression under different values of the LJ energy factor λ. The lines are the theoretical results with $\eta = 0.5$, $\bar{B} = 270$, $\bar{\gamma} = 0.136\lambda$.

The CNTs are five-layered and have approximately the same size as the CNSs under study (e.g., the innermost tube is chosen to have almost the same size as the core of the CNSs). As shown in Fig. 7(*b*), the stress-strain curves show that the rigidity of the CNT crystal is substantially higher than that of CNS crystal.

Here we have focused on the deformation behavior of a CNS crystal under uniaxial compression/decompression. In a previous study we obtained a theoretical model describing the deformation behavior of a single CNS under radial compression [24]. Under radial loading, the equation corresponding to Eq. (7) for a CNS crystal is [24]

$$\bar{p}(R_e) = -\bar{\gamma}\left(\frac{1}{\bar{r}_{0e}} + \frac{\eta}{\bar{R}_e}\right) + \frac{1}{2}\left(\frac{1}{\bar{r}_{0e}^2} - \frac{1}{\bar{R}_e^2}\right) \tag{11}$$

We conducted MD simulations to investigate if a CNS crystal would collapse under radial compression. After relaxation in the NPT ensemble, the CNS crystal shows a triangular lattice configuration (Fig. 8), which is then compressed equibiaxially at a constant strain rate. The results show that the compression forces the CNSs to contract their inner cores until they are tightly packed (Fig. 8). Once the applied load is removed, the crystal would recover to the initial state. The stress-strain curves for loading and unloading fit well with each other, indicating negligible energy dissipation compared to the uniaxial compression (Fig. 9). Compared to the uniaxial loading of a CNS crystal where the deforming mode is dominated by bending of the multiwalled graphene layers, the deforming mode of a CNS crystal under radial loading is dominated by core contraction through interlayer sliding.

Figure 9 shows that our theoretical model from Eq. (11) can fit the MD results well if the following parameters are used: $\eta = 0.5$, $\bar{B} = 270$, $\bar{\gamma} = 0.136\lambda$ (Fig. 9). Here only the parameter η is tuned to fit the MD results.

5 Summary

We have investigated the deformation behaviors of a carbon nanoscroll crystal under lateral uniaxial as well as radial compression/decompression through both MD simulations and theoretical modeling. It is found that the CNS crystal shows hysteresis behavior under uniaxial compression/decompression due to unstable collapse and snap-open of its inner core. The dissipation energy during the loading cycle can be tuned by changing the LJ interaction energy through an applied electric field. In contrast, no such hysteresis behavior is found when the same CNS crystal is subject to radial compression/decompression.

Acknowledgment

XS acknowledge the support by the National Natural Science Foundation of China (NSFC) (Grant No. 11023001) and the computation resource supported by the Supercomputing Center of Chinese Academy of Sciences (SCCAS). NMP is supported by the European Research Council Starting Grants (ERC StG) 2011 Bihsnam "Bio-inspired hierarchical super-nanomaterials." HG is supported by the Center for Mechanics and Materials (CMM) in Tsinghua University.

References

[1] Viculis, L. M., Mack, J. J., and Kaner, R. B., 2003, "A Chemical Route to Carbon Nanoscrolls," Science, **299**, p. 1361.

[2] Xie, X., Ju, L., Feng, X., Sun, Y., Zhou, R., Liu, K., Fan, S., Li, Q., and Jiang, K., 2009, "Controlled Fabrication of High-Quality Carbon Nanoscrolls From Monolayer Graphene," Nano Lett., **9**, pp. 2565–2570.
[3] Savoskin, M. V., Mochalin, V. M., Yaroshenko, A. P., Lazareva, N. I., Konstantinova, T. E., Baruskov, I. V., and Prokofiev, I. G., 2007, "Carbon Nanoscrolls Produced From Acceptor-Type Graphite Intercalation Compounds," Carbon, **45**, pp. 2797–2800.
[4] Roy, D., Angeles-Tactay, E., Brown, R. J. C., Spencer, S. J., Fry, T., Dunton, T. A., Young, T., and Milton, M. J. T., 2008, "Synthesis and Raman Spectroscopic Characterization of Carbon Nanoscrolls," Chem. Phys. Lett., **465**, pp. 254–257.
[5] Chuvilin, A. L., Kuznetsov, V. L., and Obraztsov, A. N., 2009, "Chiral Carbon Nanoscrolls With a Polygonal Cross-Section," Carbon, **47**, pp. 3099–3105.
[6] Shioyama, H., and Akita, T., 2003, "A New Route to Carbon Nanotubes," Carbon, **41**, pp. 179–181.
[7] Chen, Y., Lu, J., and Gao, Z., 2007, "Structural and Electronic Study of Nanoscrolls Rolled Up by a Single Graphene Sheet," J. Phys. Chem. C, **111**, pp. 1625–1630.
[8] Braga, S. F., Coluci, V. R., Legoas, S. B., Giro, R., Galvao, D. S., and Baughman, R. H., 2004, "Structure and Dynamics of Carbon Nanoscrolls," Nano Lett., **4**, pp. 881–884.
[9] Braga, S. F., Coluci, V. R., Baughman, R. H., and Galvao, D. S., 2007, "Hydrogen Storage in Carbon Nanoscrolls: An Atomistic Molecular Dynamics Study," Chem. Phys. Lett., **441**, pp. 78–82.
[10] Coluci, V. R., Braga, S. F., Baughman, R. H., and Galvao, D. S., 2007, "Prediction of the Hydrogen Storage Capacity of Carbon Nanoscrolls," Phys. Rev. B, **75**, p. 125404.
[11] Mpourmpakis, G., Tylianakis, E., and Froudakis, G. E., 2007, "Carbon Nanoscrolls: A Promising Material for Hydrogen Storage," Nano Lett., **7**, pp. 1893–1897.
[12] Pan, H., Feng, Y., and Lin, J., 2005, "Ab Initio Study of Electronic and Optical Properties of Multiwall Carbon Nanotube Structures Made Up of a Single Rolled-Up Graphite Sheet," Phys. Rev. B, **72**, p. 085415.
[13] Rurali, R., Coluci, V. R., and Galvao, D. S., 2006, "Prediction of Giant Electroactuation for Papyruslike Carbon Nanoscroll Structures: First-Principles Calculations," Phys. Rev. B, **74**, p. 085414.
[14] Shi, X., Pugno, N. M., and Gao, H., 2010, "Tunable Core Size of Carbon Nanoscrolls," J. Comput. Theoret. Nanosc., **7**, pp. 517–521.
[15] Shi, X., Cheng, Y., Pugno, N. M., and Gao, H., 2010, "Tunable Water Channels With Carbon Nanoscrolls," Small, **6**, pp. 739–744.
[16] Shi, X., Pugno, N. M., and Gao, H., 2010, "Mechanics of Carbon Nanoscrolls: A Review," Acta Mech. Solid. Sin., **23**(6), pp. 484–497.
[17] Cheng, Y., Shi, X., Pugno, N. M. and Gao, H., 2012, "Substrate-Supported Carbon Nanoscroll Oscillator," Physica E Low Syst. Nanost., **44**, pp. 955–959.
[18] Shi, X., Cheng, Y., Pugno, N. M., and Gao, H., 2010, "A Translational Nanoactuator Based on Carbon Nanoscrolls on Substrates," Appl. Phys. Lett., **96**, p. 053115.
[19] Shi, X., Pugno, N. M., Cheng, Y., and Gao, H., 2009, "Gigahertz Breathing Oscillators Based on Carbon Nanoscrolls," Appl. Phys. Lett. **95**, p. 163113.
[20] Zhang, Z., and Li, T., 2011, "Ultrafast Nano-Oscillators Based on Interlayer-Bridged Carbon Nanoscrolls," Nanosc. Res. Lett., **6**, p. 470.
[21] Zhang, Z., and Li, T., 2010, "Carbon Nanotube Initiated Formation of Carbon Nanoscrolls," Appl. Phys. Lett., **97**, p. 081909.
[22] Zhang, Z., Huang, Y., and Li, T., 2010, "Buckling Instability of Carbon Nanoscrolls," J. Appl. Phys., **112**, p. 063515.
[23] Huang, Y., and Li, T., 2013, "Molecular Mass Transport Via Carbon Nanoscrolls," ASME J. Appl. Mech., **80**(4), p. 041038.
[24] Shi, X., Pugno, N. M., and Gao, H., 2011, "Constitutive Behavior of Pressurized Carbon Nanoscrolls," Int. J. Fract., **171**, pp. 163–168.
[25] Pugno, N. M., 2010, "The Design of Self-Collapsed Super-Strong Nanotube Bundles," J. Mech. Phys. Solid., **58**, pp. 1397–1410.
[26] Stuart, S. J., Tutein, A. B., and Harrison, J. A., 2000, "A Reactive Potential for Hydrocarbons With Intermolecular Interactions," J. Chem. Phys., **112**, pp. 6472–6486.
[27] Plimpton, S., 1995, "Fast Parallel Algorithms for Short-Range Molecular-Dynamics," J. Comput. Phys., **117**, pp. 1–19.
[28] Elliott, J. A., Sandler, J. K. W., Windle, A. H., Young, R. J., and Shaffer, M. S. P., 2004, "Collapse of Single-Wall Carbon Nanotubes is Diameter Dependent," Phys. Rev. Lett., **92**, p. 095501.
[29] Tang, T., Jagota, A., Hui, C. Y., and Glassmaker, N. J., 2005, "Collapse of Single-Walled Carbon Nanotubes," J. Appl. Phys., **97**, p. 074310.
[30] Liu, B., Yu, M. F., and Huang, Y., 2004, "Role of Lattice Registry in the Full Collapse and Twist Formation of Carbon Nanotubes," Phys. Rev. B, **70**, p. 161402.
[31] Xiao, J., Liu, B., Huang, Y., Zuo, J., Hwang, K.-C., and Yu, M.-F., 2007, "Collapse and Stability of Single- and Multi-Wall Carbon Nanotubes," Nanotechnology, **18**(39), p. 359703.
[32] Liu, J., 2012, "Explicit Solutions for a SWCNT Collapse," Arch. Appl. Mech., **82**, pp. 767–776.